ACS APPLIED MATERIALS & INTERFACES

www.acsami.org

Research Article

Atomic Layer Deposition-Made MoS_2–ReS_2 Nanotubes with Cylindrical Wall Heterojunctions for Ultrasensitive MiRNA-155 Detection

Lei Liu,*,† Mengshu Kong,† Youqiang Xing, Ze Wu, and Yunfei Chen

Cite This: *ACS Appl. Mater. Interfaces* 2022, 14, 10081–10091

Read Online

ACCESS | Metrics & More | Article Recommendations | Supporting Information

ABSTRACT: As a member of the two-dimensional transition metal dichalcogenide family, rhenium disulfide (ReS_2) is a highly competitive favorite in the field of photoelectric sensors. Nevertheless, the rapid recombination of electron–hole pairs and poor electronic transmission capacity of pure ReS_2 limit its wider applications. As a new attempt to optimize its inherent structure and challenge its competency boundary, in this work, a bimetallic co-chamber feeding atomic layer deposition with a precise dose regulation strategy has been used to fabricate ReS_2 nanotubes (ReS_2-NTs) and MoS_2–ReS_2 heterojunction nanotubes (MoS_2–ReS_2-HNTs) based on the anodic aluminum oxide template sacrifice method for the first time. These obtained NTs have at least two advantages: they have a controllable diameter (40–500 nm), definite wall thickness (1 layer to 10 layers), and desirable Mo-to-Re ratio (0 to 90%), and their electron-transfer capacity and photocurrent response can be effectively enhanced by the incorporated Mo atoms. Further experiments indicated that MoS_2–ReS_2-HNTs with a real Mo-to-Re ratio of 31.0% exhibits the best photocurrent response performance, by which the ultrasensitive detection of cancer-related miRNA-155 with a linear range of 10 aM to 1 nM and a detection limit of 1.8 aM is achieved.

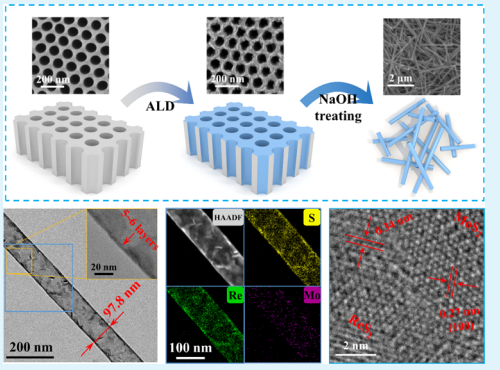

KEYWORDS: *ALD, heterojunction nanotube, ReS_2, MoS_2, biosensor*

1. INTRODUCTION

The micromechanical cleavage approach suggested in 2005 opened a window for preparing two-dimensional transition metal dichalcogenides (2D TMDs, represented as MX_2, where M = Mo, W, Re, etc.; X = S, Se, Te, etc.). 2D TMD materials have attracted more extensive attention because of their unique electrical and optical properties.[1−4] For example, when the film thickness changes from multilayer to monolayer, the band structure of some TMD materials (such as MoS_2 and WS_2) change from an indirect band gap to a direct one because of valley spin coupling, which promotes their application in optoelectronic areas.[5] Moreover, TMDs can combine with various 2D materials and result in heterojuncted structures almost without lattice-mismatch problems for better performances and wider applications.[6,7]

Early detection of cancer is an important way to improve its cure rate effectively. Fortunately, previous studies have revealed that abnormal expression at an ultralow concentration of some or a specific combination of microRNAs (miRNAs) in serum and/or other body fluids has a significant corresponding relationship with the early occurrence and evolution of cancer.[8−10] For example, miRNA-155 (a type of endogenous non-coding RNA with a sequences of 5′-UUA AUG CUA AUC GUG AUA GGG GU-3′) can been regarded as an important marker for several cancers such as non-small-cell lung cancer, breast cancer, and B-cell lymphoma.[11−13] Many other examples also show that the types of miRNAs can be used for early diagnosis and monitoring of cancer evolution, which hugely depends on their ultrasensitive detection. Among many detection methods of miRNAs, such as electrochemiluminescence (ECL),[14] differential pulse voltammetry,[15] and surface-enhanced Raman scattering,[16] photoelectrochemical (PEC) measurement based on a well-studied photon-to-electricity conversion analytical technique with a low background noise and high sensitivity is one of the most promising choices in the future.[17−20] Of course, highly sensitive detection based on PEC measurement depends on the high photoelectric conversion ability of materials.

As a member of the TMD family, rhenium disulfide (ReS_2) has a unique anisotropic structure and direct band gap from bulk to monolayer, which results in excellent optical absorptivity and carrier transmission characteristics, thus

Received: November 29, 2021
Accepted: February 7, 2022
Published: February 17, 2022

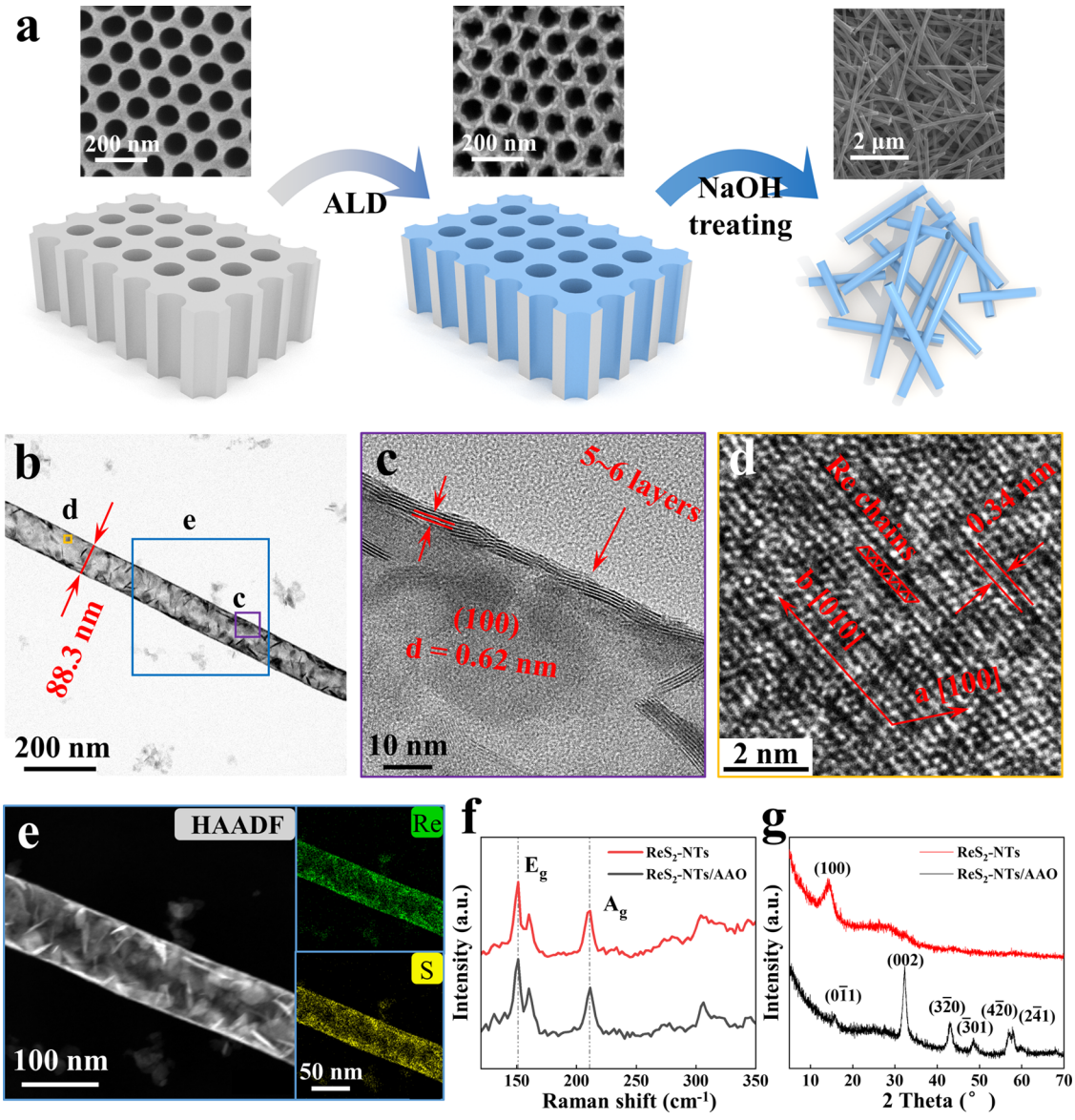

Figure 1. Characterization of ReS_2-NTs. (a) Schematic illustration of the synthesis of ReS_2-NTs; the inserts are scanning electron microscopy (SEM) images of the top view of the AAO template before and after ALD reaction and the uniformly distributed ReS_2-NTs on ITO. (b) Transmission electron microscopy (TEM) images of a single ReS_2-NT. (c,d) High-resolution transmission electron microscopy (HRTEM) images of the local parts in the corresponding areas in (b). (e) High-angle annular dark-field (HAADF) images of the area in (b) and its elemental mapping images of Re and S, respectively. (f) Raman spectra and (g) XRD patterns of the ReS_2-NTs/AAO before and after sodium hydroxide (NaOH) treatment.

making it a new favorite in the field of photoelectric sensors especially for biomedical and related areas.[21,22] Nevertheless, the rapid recombination of electron−hole pairs and poor electronic transmission capacity in pure ReS_2 have limited its wider application.[23] In order to eliminate this deficiency, many efforts such as structure optimization and composition designing have been taken to achieve modified ReS_2 materials with specific microstructures and improved properties. For example, vertically oriented arrays of ReS_2 nanosheets with large surface areas have been obtained by chemical vapor deposition, which is beneficial for improving the interaction between sensitive substances and analytes, thus effectively increasing the sensitivity for humidity detection.[24] Similarly, colloidal ReS_2 nanosheet films with a large surface area has been prepared by a less-time-consuming and costly colloidal synthesis approach for the detection of NH_3 gas.[25] Meanwhile, Ti_3C_2−ReS_2 with a heterostructure prepared by hydrothermal method indicates that Ti_3C_2 slowed the recombination of electron−hole pairs and optimized the electrical conductivity of materials, thus improving the photoelectric response of ReS_2.[26] What is more, WS_2−ReS_2 heterojunction fabricated by physical exfoliation has been found to have superior optoelectronic properties, including moderate photoresponsivity, polarization sensitivity, and fast photoresponse speed, which make it a self-driven photodetector.[27] Undoubtedly, various ways of obtaining or manufacturing ReS_2 lead to remarkable performance differences of as-prepared sensors, so it is very important to achieve more accurate and effective structure-composition coupling control by continuous innovation of the acquisition technology for 2D materials. A typical example is that atomic layer deposition (ALD) with atomic-scale accuracy has been applied in the controlled manufacture

https://doi.org/10.1021/acsami.1c23009
ACS Appl. Mater. Interfaces 2022, 14, 10081−10091

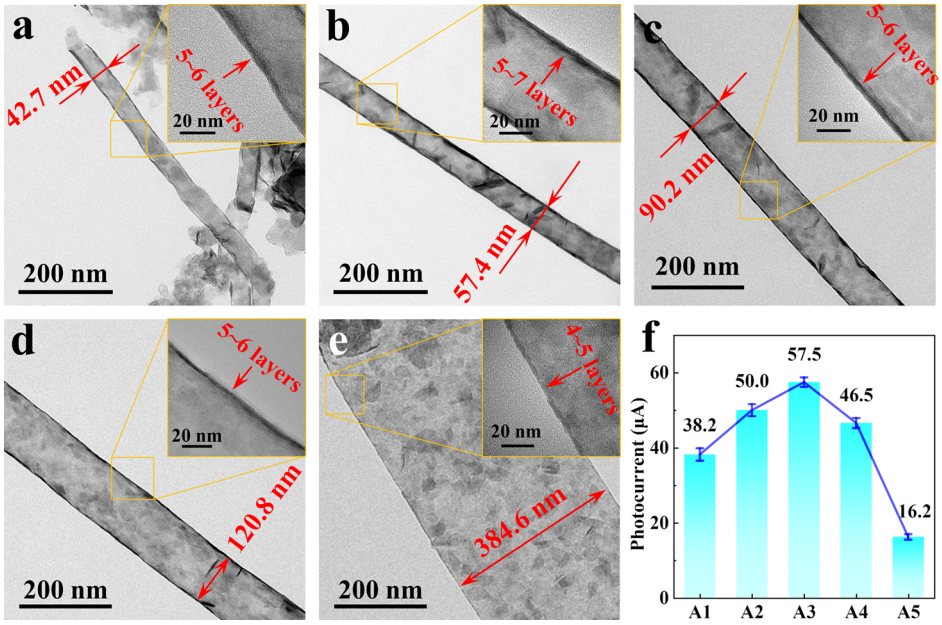

Figure 2. Characterization of ReS_2-NTs with different diameters. (a–e) TEM images of ReS_2-NTs produced by AAO of different pore sizes: (a) A1, (b) A2, (c) A3, (d) A4, and (e) A5. The inserts are the HRTEM images of the local parts in the corresponding areas. (f) Photocurrent response of ReS_2-NTs produced by AAO of different pore sizes. The number of ALD cycles is set as 90C.

of 2D ReS_2 and the comprehensive modulation of its structure and performance.[28,29] Meanwhile, anodic aluminum oxide (AAO) is widely used as the template for nanotube (NT) fabrication because of its excellent stability at high temperatures together with good uniformity in the tunable diameter and the depth of nanochannels, while it can also be easily removed to obtain pure NT products; thus, AAO is selected as the sacrificial template.[30,31]

Inspired by the advantages of ALD in ultra-precision manufacturing at an atomic scale and the strategy of low-dimensional controllable doping, in this work, ReS_2 nanotubes (ReS_2-NTs) and MoS_2–ReS_2 heterojunction NTs (MoS_2–ReS_2-HNTs) with a controllable diameter, definite wall thickness, desirable Mo-to-Re ratio, and improved properties are prepared via a bimetallic co-chamber feeding ALD for the first time based on AAO template sacrifice method, by which the ultrasensitive detection of miRNA-155 with a linear range of 10 aM to 1 nM and a detection limit of 1.8 aM is achieved.

2. RESULTS AND DISCUSSION

2.1. Fabrication of ReS_2-NTs. The schematic illustration in Figure 1a shows the overall fabrication process of ReS_2-NTs. The AAO with homogeneous nanochannels is selected as the growth template in ALD because of its excellent structural stability at high temperatures.[32] ReS_2 film is fabricated on the AAO template by general ALD methods in a vacuum chamber at 400 °C using hydrogen sulfide (H_2S) gas and sublimed rhenium pentachloride ($ReCl_5$, heated up to 110 °C) as S and Re precursors, whose morphology is confirmed by SEM. After that, a selective etching of alumina (Al_2O_3) from ReS_2-NTs is carried out in 1 M NaOH solution for 24 h at 25 °C until the template is completely etched away. Finally, the NaOH solution is repeatedly diluted and replaced with deionized water until it becomes a neutral solution.

By this way, typical ReS_2-NTs with an average diameter of 88.3 nm are obtained by TEM (Figure 1b), whose wall thickness is 5–6 layers, defined by HRTEM (Figure 1c). Furthermore, ReS_2 lattices with a spacing of 0.62 nm attributed to its (100) plane are clearly observed in HRTEM. Finally, highly oriented Re chains form in the ReS_2 film along the lattice direction of the *b*-axis. The parallel Re atom chains along the *b*[010] direction with a distance of 0.34 nm (Figure 1d) are considered a unique ReS_2 structure with a distorted 1T′-phase,[33,34] while its compositions of Re and S can be confirmed by the elemental mapping under HAADF pattern (Figure 1e).

Moreover, the peaks at 151 cm^{-1} and 211 cm^{-1} in Raman spectra can be attributed to the in-plane (E_g) and out-of-plane (A_g) vibrational modes of ReS_2 (Figure 1f),[35] in which limited signal changes between ReS_2-NTs attached on the AAO template by in situ growth (ReS_2-NTs/AAO) and independent ReS_2-NTs removed from the AAO template can be found. However, X-ray diffraction (XRD) spectrum for ReS_2-NTs/AAO reflects 6 additional peaks at 15.72, 32.28, 43.03, 48.56, 57.02, and 57.93° compared with that for ReS_2-NTs (Figure 1g), corresponding to $(0\bar{1}1)$, (002), $(3\bar{2}0)$, $(\bar{3}01)$, $(4\bar{2}0)$, and $(2\bar{4}1)$ planes of the triclinic ReS_2.[36] In contrast, the diffraction peak at 14.34° corresponding to the (100) plane appears, while other peaks become weaker or even disappear after removing the AAO template. On further examination of their microstructure, ReS_2-NTs/AAO contain both in-plane and out-of-plane flakes in an ordered arrangement (Figure S1), while unsupported ReS_2-NTs have a random distribution (insert in Figure 1a). The peak intensity depends largely on the growth orientation of crystals: different growth environments (outer and inner surface of AAO) can lead to different growth orientations of ReS_2; thus, a significant change in XRD signals appears after the ReS_2-NTs are released from AAO.

Generally, the diameter of NTs largely depends on the pore size of the AAO template; thus, five types of AAO with different pore sizes are taken to control the diameters of ReS_2-NTs, and the ALD cycles are set as 90C.[37,38] Here, AAO templates with different size parameters are named AAO-1, AAO-2, AAO-3, AAO-4, and AAO-5 (Figure S2), while the

https://doi.org/10.1021/acsami.1c23009
ACS Appl. Mater. Interfaces 2022, 14, 10081–10091

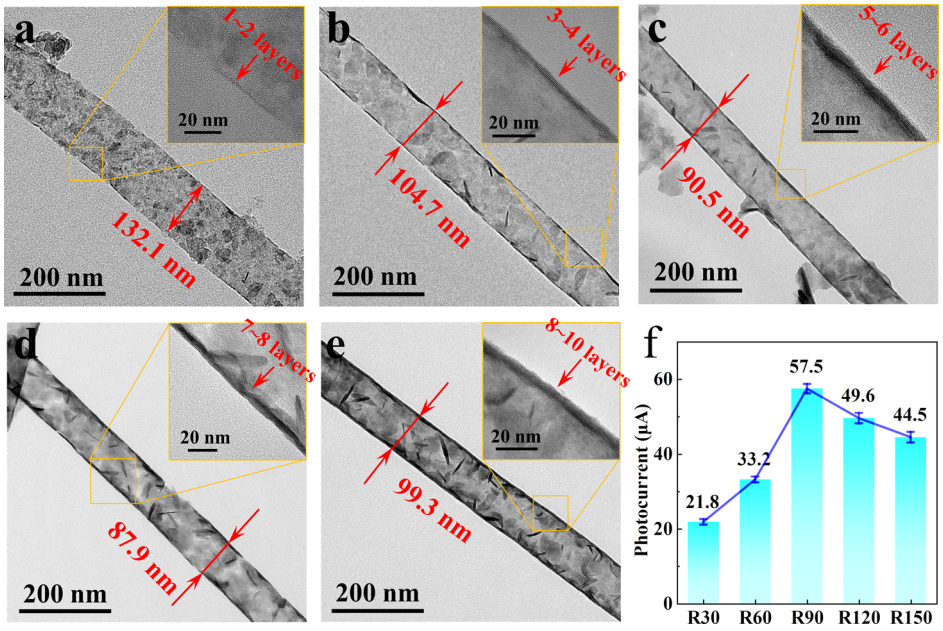

Figure 3. Characterization of ReS_2-NTs with different ALD cycles. (a–e) TEM images of ReS_2-NTs produced by ALD cycles set as 30, 60, 90, 120, and 150 cycles, marked as R30, R60, R90, R120, and R150, respectively. The insert is the HRTEM images of the local parts in the corresponding areas. (f) Photocurrent response of ReS_2-NTs produced by different ALD cycles. AAO-3 is taken as the template.

corresponding as-prepared ReS_2-NTs obtained by 90 ALD cycles are named A1, A2, A3, A4, and A5, respectively (Figure 2a–e). By this way, typical ReS_2-NTs with different diameters are obtained, whose wall thickness is 5–6 layers (insert in Figure 2a–e). The diameter of A5 (Figure 2e) is 384.6 nm, while the diameter of its corresponding AAO template is only 310 nm. There may be two reasons for the dimensional difference between the NTs and their templates: On the one hand, the diameter of NTs may change slightly after they get rid of the binding with templates. On the other hand, their larger diameter and lesser wall thickness may cause elliptical distortion in the cross section of the original ideal cylindrical NTs (Figure S3); thus, there is a significant increase in diameter as viewed from the direction perpendicular to the long axis of the ellipse.

The size dimensional changes in these ReS_2-NTs determine their performance differences; therefore, electrochemical impedance spectroscopy (EIS) test results indicate that the electron transfer resistance (R_{ct}) values for A1, A2, A3, A4, and A5 are 78.6, 82.9, 77.5, 79.5, and 98.9 Ω, respectively (Figure S4).[37] The significant increase in the last R_{ct} for A5 reflects its lower electron transfer ability, just because its larger diameter (384.6 nm) and lesser wall thickness (4–5 layers) cannot maintain a perfect cylindrical structure and deforms into an elliptic cylinder. Meanwhile, the effective surface area (ESA) values obtained from chronocoulometry (CC) test for indium tin oxide (ITO), A1, A2, A3, A4, and A5 are 0.24, 0.56, 1.01, 0.80, 0.86, and 0.27 cm^2, respectively (Figure S5).[39] Obviously, A3 has the highest ESA value (1.01 cm^2), which can provide more active sites to accelerate the electron transfer. The ESA values of these ReS_2-NTs depend largely on the three-dimensional (3D) structure of their constituent units: the larger diameter and thinner wall of A5 lead to radial distortion of NTs (Figure S3), while smaller diameter of A1 makes the NTs easy to agglomerate after the inner stress-induced cracking, which has been confirmed by density-functional theory calculations.[40] Based on the above experimental results, A3 has the greatest overall performance advantage (57.5 μA); thus, AAO-3 has been selected as the standard template for further research (Figures 2f and S6).

Furthermore, the wall thickness of ReS_2-NTs can be modulated by ALD cycles, and AAO-3 is taken as the growth template (Figure 3a–e). ReS_2-NTs produced by 30, 60, 90, 120, and 150 ALD cycles are named R30, R60, R90, R120, and R150, respectively. According to our experiment, the out-of-plane growth of ReS_2 starts from R60 (Figure S7),[29] and there is a good linear dependence between the wall thickness and the ALD cycle (insert in Figures 3a–e and S8), which indicates that the ALD method has good controllability for the thickness of NTs.[41] Moreover, R30 has a larger diameter (132.1 nm) compared with others due to the ellipse distortion caused by its thin wall (Figures 3a and S9).

Similarly, R_{ct} values for R30, R60, R90, R120, and R150 are 90.3, 77.1, 77.5, 77.4, and 73.7 Ω, respectively (Figure S10), which indicates that R30 has the weakest electron transfer ability, which is also due to the elliptical distortion of the NT structure caused by its super-thin wall (1–2 layers, Figure S9). In addition, the ESA values of R30, R60, R90, R120, and R150 are 0.33, 0.57, 1.01, 0.91, and 0.81 cm^2, respectively (Figure S11). By definition, ESA refers to the total surface area of a material per unit mass on ITO. Therefore, when the wall of ReS_2-NTs is thickened and their diameter remains almost unchanged, the number of NTs per unit mass is reduced, so their ESA is reduced. In addition, the thinner wall can lead to the radial distortion of ReS_2-NTs, which destroys the 3D structure of its constituent units, thus reducing ESA values. Based on the above experimental results, R90 has the best photocurrent response (57.5 μA); thus, 90 ALD cycles are used for further research (Figures 3f and S12).

2.2. Fabrication of MoS_2–ReS_2-HNTs. Based on the previous optimization, AAO-3 is used as the basic template and 90 ALD cycles are used as the basic parameters in fabricating MoS_2–ReS_2-HNTs. A bimetallic co-chamber feeding ALD method is used to prepare MoS_2–ReS_2-HNTs by a precise

https://doi.org/10.1021/acsami.1c23009
ACS Appl. Mater. Interfaces 2022, 14, 10081–10091

dose regulation strategy (Table 1).[42] In each sample, 90 ALD cycles are separated evenly into 6 "super-cycles", and then, 5

Table 1. Detailed Fabrication Information of MoS_2−ReS_2-HNTs[a]

sample ID	one super-cycle	repeat time	Mo-to-Re feed ratio (R_{fr})	Mo-to-Re real ratio (R_{rr})
RM1	15 ReS only	6	0	0
RM2	14 ReS followed by 1 ReMoS		6/90 (6.7%)	7.5 ± 0.3%
RM3	10 ReS followed by 5 ReMoS		30/90 (33.3%)	31.0 ± 4.5%
RM4	5 ReS followed by 10 ReMoS		60/90 (66.7%)	58.7 ± 5.5%
RM5	15 ReMoS		90/90 (100%)	90.5 ± 10.0%

[a]ReS, one $ReCl_5$ pulse followed by one H_2S pulse; ReMoS, one $ReCl_5$ and one $MoCl_5$ pulse are applied simultaneously, followed by one H_2S pulse.

parallel samples (RM1, RM2, RM3, RM4, and RM5) are set according to the different ratio of ReS to ReMoS in each "super-cycle". The Mo-to-Re feed ratio (R_{fr}) refers to the proportion of ReMoS in 90 ALD cycles, while the Mo-to-Re real ratio (R_{rr}) is taken from EDS element mapping.

As shown in their TEM images, the morphology of MoS_2−ReS_2-HNTs does not change significantly after the introduction of different contents of MoS_2 (Figures 4a and S13a−c). The wall thickness of these NTs is 5−6 layers, which shows that the effect of different feed ratios of the Re source and Mo source on the growth rate of NTs is quite limited. Element mapping in the HAADF mode shows the uniform mixing of MoS_2 and ReS_2 in RM3, and the pixel points corresponding to Mo atoms in RM2, RM3, RM4, and RM5 increase gradually,

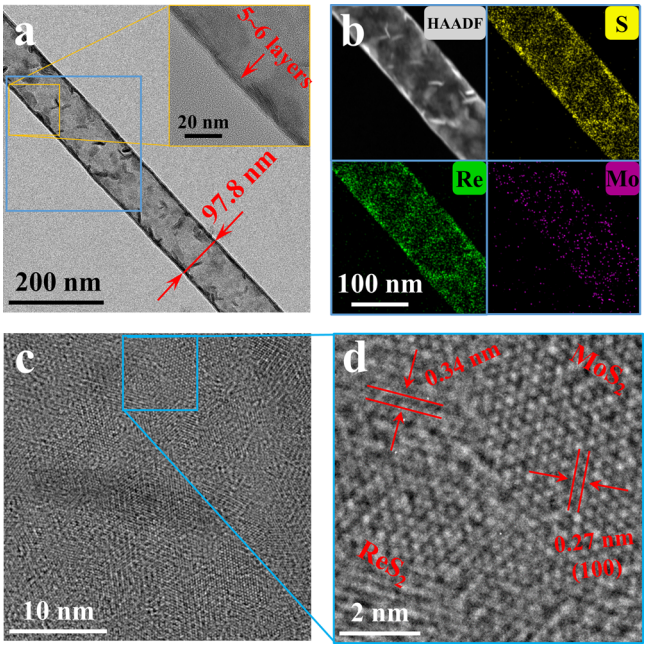

Figure 4. TEM characterization of MoS_2−ReS_2-HNTs. (a) TEM images of RM3. The insert is the HRTEM image of the local parts in the corresponding area. (b) HAADF image of the area in (a) and its elemental mapping images of S, Re, and Mo. (c) AC-HRTEM image of MoS_2−ReS_2-HNTs. (d) Enlarged HRTEM image of the lateral heterojunction.

which is consistent with the increasing feed ratio of the Mo source (Figures 4b and S13d−f). Moreover, the formation of the lateral MoS_2−ReS_2 heterojunction on the wall of the heterojuncted NTs (Figure 4c,d) indicates that the reaction in the ALD is more likely to occur between the same compounds.[43]

Furthermore, the average Mo-to-Re real ratios (R_{rr}) obtained by element mapping are 0% (RM1), 7.5% (RM2), 31.0% (RM3), 58.7% (RM4), and 90.5% (RM5) corresponding to the Mo-to-Re feed ratios (R_{fr}) of 0, 6.7, 33.3, 66.7, and 100%, respectively (Table 1). The R_{rr} values are slightly lower than their theoretical values and can be assigned to the difference in the optimum reaction temperature for ReS_2 (400 °C) and MoS_2 (460 °C).[28,44] Obviously, the reaction temperature used in ALD makes the Re precursor easier to grab the limited nucleation sites, thus leading to a higher element ratio.

The Re 4f-related X-ray photoelectron spectroscopy (XPS) peaks in RM1 (pure ReS_2-NTs) at 42.3 and 44.7 eV correspond to Re $4f_{7/2}$ and Re $4f_{5/2}$ (Figure 5a),[45] while those peaks for RM3 and RM5 show a uniform shift toward lower binding energies (0.5 eV for RM3 and 0.4 eV for RM5) due to the increase in their electron density.[46] The same shifts toward the low binding energy direction (0.3 eV for RM3 and 0.2 eV for RM5) also occur in those for S 2p-related peaks (Figure 5b). After Mo incorporation, the S 2s-related peak shifts from 227.1 to 226.5 eV and the Mo 3d-related peak appears (Mo $3d_{5/2}$ at 228.6 eV and Mo $3d_{3/2}$ at 231.8 eV) in RM3, which indicate the formation of Mo−S bonds (Figure 5c).[33] Compared with the XPS signals in RM1, the downshifts of core-level Re- and S-related peaks in RM3 strongly indicate the charge transfer from MoS_2 to ReS_2.[46,47] Moreover, with the enlargements of the Mo elements in RM5, an obvious additional peak appears at Mo $3d_{5/2}$ with 0.9 eV upshift, indicating the mixed 1T′ phase and 2H phase of the introduced MoS_2 (1T′-MoS_2 and 2H−MoS_2) (Figure 5c).[48] Meanwhile, the S 2p-related peak in RM5 for the heterojunctions of 2H−MoS_2 and 1T′-ReS_2 can be separated into two peaks (S $2p_{3/2}$ at 162.5 eV and S $2p_{1/2}$ at 163.5 eV),[48,49] and the other two peaks (orange dashed peaks, S $2p_{3/2}$ at 161.8 eV and S $2p_{1/2}$ at 162.8 eV) located at lower binding energies shifted by 0.7 eV with reference to 2H−MoS_2 belong to 1T′-MoS2 (Figure 5b).[50] In addition, comparing the XPS signals of RM3 and RM5 in the Mo 3d region, the Mo 3d-related peaks (red and purple peaks) in RM3 should belong to 1T′-MoS_2 because of the slight energy difference (0.1 eV) compared with that of RM5 (Figure 5c). Therefore, two additional XPS peaks at 161.7 and 162.7 eV are found in the S 2p region of RM3 corresponding to 1T′-MoS_2 (Figure 5b). Furthermore, such weak or even disappeared E_{2g}^1 mode in MoS_2−ReS_2-HNTs verifies the existence of MoS_2 with the 1T′ phase, while the existence of the 2H phase is confirmed by lattice characterization (Figures 4d and 5d).[48] The formation of the metastable 1T′ phase may result from the stress that is caused by the coupling effect of MoS_2 and ReS_2,[51] while the formation of the semiconducting 2H phase can be attributed to the stability of the 2H phase in the sample with more Mo atoms.[52]

Accordingly, Raman peaks at 376 and 404 cm^{-1} correspond to E_{2g}^1 and A_{1g} vibration modes in MoS_2, respectively,[53] which begin to appear in RM2 (Figure 5d). With the gradual enlargements of the feeding proportion for the Mo source, the peak intensity at 404 cm^{-1} shows a sustained increase,

https://doi.org/10.1021/acsami.1c23009
ACS Appl. Mater. Interfaces 2022, 14, 10081−10091

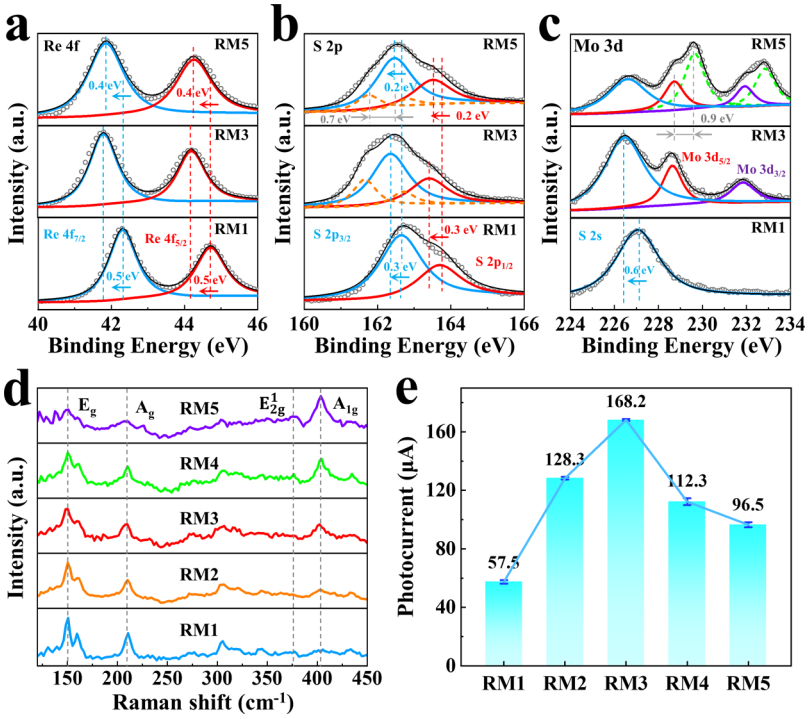

Figure 5. Characterization of MoS_2−ReS_2-HNTs. XPS spectra of Re 4f (a), S 2p (b), and Mo 3d (c) of RM1, RM3, and RM5. (d) Raman spectra of MoS_2−ReS_2-HNTs. (e) Photocurrent response of MoS_2−ReS_2-HNTs.

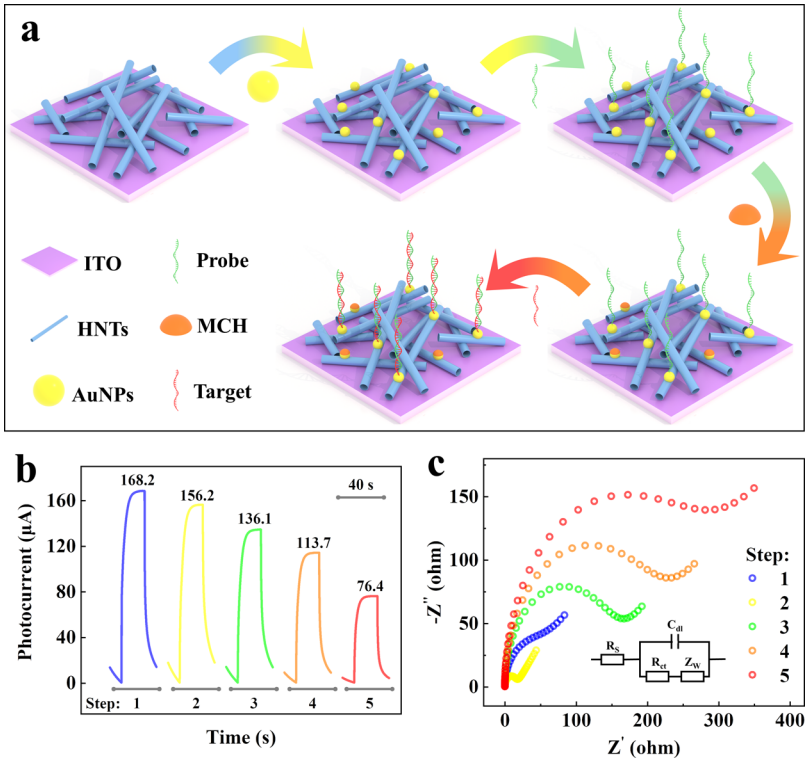

Figure 6. Fabrication of PEC biosensors. (a) Illustration of the proposed PEC biosensor for miRNA-155 detection. (b,c) Photocurrent response and EIS images of different electrodes during the built-up of the sensing platform in which MoS_2−ReS_2-HNTs/ITO, AuNPs/MoS_2−ReS_2-HNTs/ITO, probe/AuNPs/MoS_2−ReS_2-HNTs/ITO, MCH/probe/AuNPs/MoS_2−ReS_2-HNTs/ITO, and miRNA-155/MCH/probe/AuNPs/MoS_2−ReS_2-HNTs/ITO are steps 1−5, respectively.

reflecting the continuous expansion of the MoS_2 component in these MoS_2−ReS_2-HNTs.

As a result, the EIS results show that R_{ct} values for RM1, RM2, RM3, RM4, and RM5 are 77.5, 61.4, 51.6, 89.4, and 120.0 Ω, respectively (Figure S14). The significant decrease in the value for RM3 indicates that suitable doping ratio can decrease R_{ct} because of the introduced MoS_2 with the metallic 1T′ phase, thus improving the photocurrent response.

https://doi.org/10.1021/acsami.1c23009
ACS Appl. Mater. Interfaces 2022, 14, 10081−10091

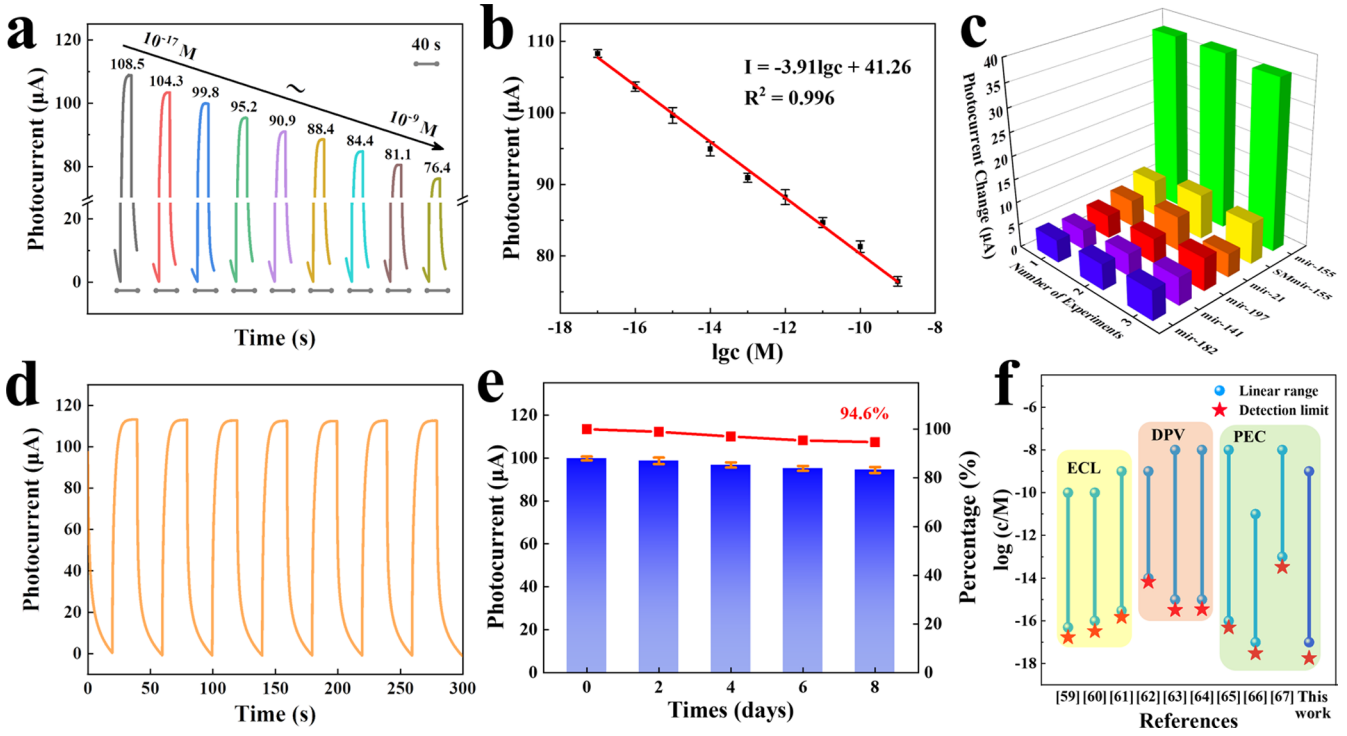

Figure 7. Performance of MoS_2−ReS_2-HNT-based biosensors. (a) Photocurrent response to different concentrations of miRNA-155 from 10 aM to 1 nM. (b) Calibration curve of the photocurrent versus logarithm value of miRNA-155 concentration. Error bars represent standard deviations of three experiments. (c) Photocurrent change in the PEC biosensor toward miRNA-155, miRNA-21, miRNA-197, miRNA-141, and miRNA-182 (10^{-9} M) detection. (d) Stability of the photocurrent response in 0.1 M PBS containing 0.1 M AA with light on and off. (e) Stability of the prepared biosensor after 8 day storage: 0 day, 2 days, 4 days, 6 days, and 8 days at 4 °C in a vacuum. (f) Obtained results of this work and other studies devoted to miRNA-155 detection.

Meanwhile, the lattice difference between MoS_2 and ReS_2 would result in a lattice mismatch, which can prevent the recombination of hole−electron pairs to enhance photocurrent response.[43]

The charge transfer from MoS_2 to ReS_2 proved by XPS (Figure 5a−c) is in line with the research results of the band structure of the MoS_2−ReS_2 heterojunction. In detail, the conduction band minimum (CBM), valence band maximum (VBM), and work function are 4.68, 6.05, and 5.1 eV for ReS_2 and 4.21, 5.56, and 4.50 eV for MoS_2, respectively.[54−56] Because of the higher CBM value of MoS_2, the electron is more likely to transfer from MoS_2 to ReS_2 under light illumination (Figure S15).[57] Meanwhile, the staggered gap structure indicates that MoS_2−ReS_2 heterojunction is a type II heterojunction, which is advantageous for preventing the recombination of hole−electron pairs with long-lived interlayer excitons, thus improving the PEC performance.[58]

Due to the above favorable factors, RM3 shows the most excellent photocurrent response (168.2 μA), which is almost 2.9 times more than that of ReS_2-NTs (Figures 5e and S16). Thus, RM3 is used in the ultrasensitive biosensor for miRNA-155 detection.

2.3. Ultrasensitive MiRNA-155 Detections. As illustrated in Figure 6a, AuNPs are deposited on RM3/ITO to immobilize the probe by forming Au−S bonds. The electrodeposition of AuNPs on the electrode surface results in a slight decrease in photocurrent (156.2 μA, Figure 6b), which can be attributed to the following: the repulsion objectively exists between negative charge on both AuNPs and ascorbic acid (AA); the accumulation of AuNPs can result in an obvious decrease in R_{ct} together with the increase in charge transfer capacity (Figures 6c and S16), thus favoring increase in photocurrent. The slight current decrease results from the coupling effects of the above two aspects. What is more, the photocurrent continues to drop as 20 μL of 1 μM probe (136.1 μA), 20 μL of 1 mM 6-mercaptohexanol (MCH) (113.7 μA), and 20 μL of 1 nM miRNA-155 (76.4 μA) are separately added in turn and R_{ct} increases gradually (Figure 6c). The negatively charged probe and target RNA can prevent the charge transfer, while the short alkanethiol of MCH blocks electron transfer from the solution to electrodes. In addition, the photocurrent continues to decline until the hybridization time reaches 2 h, indicating that it is enough for the full hybridization of the target and probe. Meanwhile, the lowest PEC value appears at an incubation temperature of 37 °C, which is consistent with the normal human body temperature. In this way, the hybridization time and the incubation temperature are optimized experimentally (Figure S18).

Furthermore, based on the above platform, miRNA-155 can be effectively detected from 10 aM to 1 nM (Figure 7a). The photocurrent gradually decreases with the increase in target concentration because of the gradual increase in steric hindrance caused by more miRNA-155 blocking the diffusion of AA. Meanwhile, from the linear relationship between the photocurrent (I) and the logarithm for the concentration of miRNA-155 (c) (Figure 7b), $I = -3.91 \log c + 41.26$ can be obtained with the correlation coefficient $R^2 = 0.996$ and a detection limit of 1.8 aM (S/N = 3). The detection specificity is then compared by 4 other types of miRNA at 1 nM (Figure 7c), among which the photocurrent change in miRNA-155 (37.3 μA) is much higher than that in miRNA-21 (6.1 μA), miRNA-197 (5.8 μA), miRNA-141 (5.1 μA), and miRNA-182

https://doi.org/10.1021/acsami.1c23009
ACS Appl. Mater. Interfaces 2022, 14, 10081−10091

(5.7 μA), which indicates that this sensing platform has a high selectivity for miRNA-155. Furthermore, according to previous research, miRNA-155 can disperse stably in the serum of lung cancer patients, which makes it a potential tumor marker for lung cancer detection. In order to verify the possibility of applying our experimental results and our sensing platform to real samples, related experimental work on the human serum samples are carried out. Three samples containing 10 pM, 0.1 pM, and 1 fM miRNA-155 (Table S1) show that their recoveries are 101.3, 99.8, and 97.1, respectively. Moreover, the corresponding RSD is less than 6%, which shows good performance in real biological samples of the as-fabricated sensing platform.

In addition, the stability test is conducted by putting the light signal on and off 7 times during 300 s, which shows only a 0.3% drop (Figure 7d). On the other hand, the modified electrodes are kept in dark at 4 °C for 8 days to test their long-term stability, and it maintains 94.6% of its initial photocurrent intensity for 1 fM miRNA-155 (Figure 7e), which indicates its outstanding storage stability.

Finally, compared with previous reports for miRNA-155 detection (Figure 7f), the sensing platform based on MoS_2−ReS_2-HNTs in this paper has a wider detection linear range (1 nM−10 aM) and a better estimated detection limit (1.8 aM),[59−67] which is potentially useful for the early diagnosis of cancer. On the other hand, the bimetallic co-chamber feeding AAO template sacrifice method is a controllable method for large-scale manufacture, which is conducive to the practical application needs in the future.

3. CONCLUSIONS

In summary, ReS_2-NTs and MoS_2−ReS_2-HNTs with a controllable diameter (from 40 to 500 nm), definite wall thickness (from 1 layers to 10 layers), and desirable Mo-to-Re ratio (from 0 to 90%) were fabricated via an accurate bimetallic co-chamber feeding ALD strategy for the first time based on AAO template sacrifice. MoS_2−ReS_2-HNTs with a real Mo-to-Re ratio of 31.0% exhibited the best photocurrent response performance, by which the ultrasensitive detection of cancer-related miRNA-155 with a linear range of 10 aM to 1 nM and a detection limit of 1.8 aM were achieved.

4. EXPERIMENTAL SECTION

4.1. Reagents and Materials. AAO templates were obtained from Pu-Yuan Nanotechnology Co., Ltd. (Hefei, China). ITO slices (3−4 Ω) were purchased from Shang Guluo Glass Co., Ltd. (Luoyang, China). Rhenium pentachloride ($ReCl_5$) was purchased from China Rhenium Co., Ltd. (Zhuzhou, China). Hydrogen sulfide (H_2S), oxygen (O_2), and nitrogen (N_2) were supplied by Nanjing Special Gas Co., Ltd. (Nanjing, China). Sodium hydroxide (NaOH), molybdenum chloride ($MoCl_5$), hydrogen tetrachloroaurate trihydrate ($HAuCl_4{\cdot}3H_2O$), 6-mercaptohexanol (MCH), phosphate buffer solution (PBS), AA, potassium hexacyanoferrate (III) ($K_3[Fe(CN)_6]$), and potassium hexacyanoferrate (II) ($K_4[Fe(CN)_6]$) trihydrate were purchased from Sigma-Aldrich (Shanghai, China). All of the reagents were purchased from Aladdin Co., Ltd. and were not further processed. The oligonucleotide sequences were provided by Sangon Biotech Co., Ltd. (Shanghai, China), and their sequences were as follows:

Probe SH-RNA: 5′-SH-ACC CCU AUC ACG AUU AGC AUU AA-3′

MiRNA-155: 5′-UUA AUG CUA AUC GUG AUA GGG GU-3′

MiRNA-21: 5′-UAG CUU AUC AGA CUG AUG UUG A-3′

MiRNA-182: 5′- UUU GGC AAU GGU AGA ACU CAC ACU -3′

MiRNA-141: 5′-UAA CAC UGU CUG GUA AAG AUG G-3′

MiRNA-197: 5′-UUC ACC ACC UUC UCC ACC CAG C-3′

Diethyl pyrocarbonate (DEPC) water was used for the preparation of all solutions to reduce the effect of RNase on the experimental results.

4.2. Preparation of ReS_2-NTs and MoS_2−ReS_2-HNTs. ReS_2-NTs/AAO and MoS_2−ReS_2-HNTs/AAO were deposited in a homemade and multisource controllable ALD setup operated under reduced nitrogen pressure. $ReCl_5$, $MoCl_5$, and H_2S were used as precursors for the deposition. According to our previous work, 400 °C is identified as the optimal temperature for ReS_2 films. The solid $ReCl_5$ and $MoCl_5$ precursors were kept at 110 °C and delivered into the reaction chamber with a N_2 carrier flow of 50 sccm.

MoS_2−ReS_2-HNTs/AAO was prepared by combining ReS_2 and MoS_2 ALD processes into a "super-cycle" (Table 1). One "super-cycle" containing 15 ALD cycles was designed by pulsing $ReCl_5$ and $MoCl_5$−$ReCl_5$ precursors successively into the same ALD chamber. Each $MoCl_5$−$ReCl_5$ cycle included $MoCl_5$−$ReCl_5$ pulsing (1 s), N_2 purging (60 s), H_2S pulsing (1 s), and N_2 purging (60 s). Meanwhile, $ReCl_5$ and $MoCl_5$ were injected into the reaction chamber together to obtain well-mixed MoS_2−ReS_2 heterojunctions. Furthermore, ReS_2-NTs/AAO was deposited by ALD without Mo source. Before being used, the AAO template was washed 3 times with acetone, ethanol, and deionized water; oven-dried at 60 °C; and then treated with O_2 plasma for 5 min.

ReS_2-NTs and MoS_2−ReS_2-HNTs were fabricated by putting ReS_2-NTs/AAO and MoS_2−ReS_2-HNTs/AAO into 1 M NaOH solution for 24 h. After that, NaOH solution was repeatedly diluted and replaced with deionized water until it was a neutral solution. Finally, ReS_2-NTs and MoS_2−ReS_2-HNTs were dried, and their suspension (1 mg/mL) was prepared by deionized water.

4.3. Fabrication of PEC-Sensing Platform. The fabrication of MoS_2−ReS_2-HNT-based PEC biosensor is depicted in Figure 6a. ITO substrates were cleaned by sonication in acetone, ethanol, and deionized water for 20 min successively and dried under N_2. ITO (5 mm × 5 mm) was first coated with 15 μL of as-prepared MoS_2−ReS_2-HNT suspension and then dried in a dark environment for 24 h. The obtained electrode was denoted as MoS_2−ReS_2-HNTs/ITO. By controlling the deposition potential at - 0.2 V and deposition time at 300 s in $HAuCl_4$ (0.1%), AuNPs prepared by electrodeposition have good uniformity. The obtained electrode was denoted as AuNPs/MoS_2−ReS_2-HNTs/ITO. The electrodes were washed with PBS solution 3 times and then dried at room temperature. After that, 20 μL of the probe immobilization buffer (1 μM) was dropped onto the electrodes (named probe/AuNPs/MoS_2−ReS_2-HNTs/ITO) and incubated for 8 h in a dark environment. Then, 20 μL of MCH (1 mM) was dropped onto the surface of the prepared electrodes for 60 min to fill unreacted AuNPs and block any nonspecific adsorption site. miRNA-155 (20 μL) with a certain concentration was dropped onto the surface of electrodes and incubated for 120 min at 37 °C. The obtained electrode was denoted as miRNA-155/MCH/probe/AuNPs/MoS_2−ReS_2-HNTs/ITO. Finally, the electrodes were washed with PBS and used as PEC anodes for PEC measurements.

4.4. Characterization. The morphology of NTs and AAO was examined by SEM (FEI Inspect F50, USA). The diameter, thickness, and EDS element mapping measurement of the NTs were identified by HRTEM (Talos F200X, ThermoFisher). The heterojunction structure of MoS_2−ReS_2-HNTs was observed by TEM (Titan 80-300, USA). The composition and crystal structures of NTs were investigated by Raman spectroscopy (Raman, LabRAM HR UV−visible) with a 532 nm laser and XRD (SmartLab, Japan). The composition and chemical bonds of the surface layer of MoS_2−ReS_2 heterojunction films were analyzed by XPS (Nexsa, ThermoFisher) with the Al Kα radiation line (1486.6 eV) and a voltage of 12 kV. All the binding energies of XPS spectra were calibrated using the C 1s (284.8 eV) of ambient hydrocarbons, and peak fitting was completed using the XPSPEAK41 software. The AAO substrates were treated with O_2 by a PCE-6 plasma cleaner.

PEC and electrochemical measurements were taken on an electrochemical workstation (CHI660E, China) with a conventional three-electrode system consisting of a saturated calomel electrode as

https://doi.org/10.1021/acsami.1c23009
ACS Appl. Mater. Interfaces 2022, 14, 10081−10091

the reference electrode, a modified ITO (0.25 cm^2) as the working electrode, and a platinum (Pt) wire as the counter electrode. All the PEC measurements were taken at an applied potential of 0.1 V under monochromatic light (1 W, 450 nm, 92 $mW \cdot cm^{-2}$) in 0.1 M PBS (pH = 7.4) containing 0.1 M AA as the electron donor. The cyclic voltammetry (CV) measurements were taken in 5 mM $[Fe(CN)_6]^{3-/4-}$ containing 0.1 M potassium chloride (KCl) solution between −0.1 and 0.6 V. EIS measurements were taken in 5.0 $mmol \cdot L^{-1}$ $[Fe(CN)_6]^{3-/4-}$ and 0.1 $mol \cdot L^{-1}$ KCl solution from 100 kHz to 0.1 Hz, and all the obtained data were processed by ZSimpWin. The effective surface was tested by CC in 0.1 mM $K_3[Fe(CN)_6]$ with 1.0 M KCl.

■ ASSOCIATED CONTENT

Supporting Information

The Supporting Information is available free of charge at https://pubs.acs.org/doi/10.1021/acsami.1c23009.

SEM images of AAO of different pore sizes and ReS_2-NTs/AAO with different ALD cycles; schematic illustration of the cross section of the NT; detailed characterizations (EIS, CC, and PEC response); relationship between ALD cycles and thickness of ReS_2-NTs; more TEM images of MoS_2−ReS_2-HNTs; schematic diagram of the band structure and charge transfer route of MoS_2−ReS_2 heterojunctions; CV images of different electrodes during the built-up of the sensing platform; parameter optimization of hybridization time and incubation temperature; and details of MiRNA-155 detection in human sera with the prepared biosensor (PDF)

■ AUTHOR INFORMATION

Corresponding Author

Lei Liu − *School of Mechanical Engineering, Southeast University, Nanjing 211189, People's Republic of China;* orcid.org/0000-0001-6202-9966; Email: liulei@seu.edu.cn

Authors

Mengshu Kong − *School of Mechanical Engineering, Southeast University, Nanjing 211189, People's Republic of China*

Youqiang Xing − *School of Mechanical Engineering, Southeast University, Nanjing 211189, People's Republic of China*

Ze Wu − *School of Mechanical Engineering, Southeast University, Nanjing 211189, People's Republic of China*

Yunfei Chen − *School of Mechanical Engineering, Southeast University, Nanjing 211189, People's Republic of China;* orcid.org/0000-0002-8682-868X

Complete contact information is available at: https://pubs.acs.org/10.1021/acsami.1c23009

Author Contributions

†L.L. and M.K. contributed equally to this work.

Notes

The authors declare no competing financial interest.

■ ACKNOWLEDGMENTS

This work was financially supported by the National Natural Science Foundation of China (52130510, 62071120, and 51822501) and the Natural Science Foundation of Jiangsu Province (BK20202006).

■ REFERENCES

(1) Fu, Q.; Han, J.; Wang, X.; Xu, P.; Yao, T.; Zhong, J.; Zhong, W.; Liu, S.; Gao, T.; Zhang, Z.; Xu, L.; Song, B. 2D Transition Metal Dichalcogenides: Design, Modulation, and Challenges in Electrocatalysis. *Adv. Mater.* **2020**, *33*, 1907818.

(2) Li, G.; Zhang, Y.-Y.; Guo, H.; Huang, L.; Lu, H.; Lin, X.; Wang, Y.-L.; Du, S.; Gao, H.-J. Epitaxial Growth and Physical Properties of 2D Materials beyond Graphene: from Monatomic Materials to Binary Compounds. *Chem. Soc. Rev.* **2018**, *47*, 6073−6100.

(3) Yin, X.; Tang, C. S.; Zheng, Y.; Gao, J.; Wu, J.; Zhang, H.; Chhowalla, M.; Chen, W.; Wee, A. T. S. Recent Developments in 2D Transition Metal Dichalcogenides: Phase Transition and Applications of the (Quasi-)Metallic Phases. *Chem. Soc. Rev.* **2021**, *50*, 10087−10115.

(4) Novoselov, K. S.; Jiang, F.; Booth, T. J.; Khotkevich, V. V.; Morozov, S. V.; Geim, A. K. Two-dimensional Atomic Crystals. *Proc. Natl. Acad. Sci. U.S.A.* **2005**, *102*, 10451−10453.

(5) Tebyetekerwa, M.; Zhang, J.; Xu, Z.; Truong, T. N.; Yin, Z.; Lu, Y.; Ramakrishna, S.; Macdonald, D.; Nguyen, H. T. Mechanisms and Applications of Steady-State Photoluminescence Spectroscopy in Two-Dimensional Transition-Metal Dichalcogenides. *ACS Nano* **2020**, *14*, 14579−14604.

(6) Li, Z.; Yao, Z.; Haidry, A. A.; Luan, Y.; Chen, Y.; Zhang, B. Y.; Xu, K.; Deng, R.; Duc Hoa, N.; Zhou, J.; Ou, J. Z. Recent Advances of Atomically Thin 2D Heterostructures in Sensing Applications. *Nano Today* **2021**, *40*, 101287.

(7) Zhang, R.; Li, M.; Li, L.; Wei, Z.; Jiao, F.; Geng, D.; Hu, W. The More, the Better−Recent Advances in Construction of 2D Multi-Heterostructures. *Adv. Funct. Mater.* **2021**, *31*, 2102049.

(8) Lu, J.; Getz, G.; Miska, E. A.; Alvarez-Saavedra, E.; Lamb, J.; Peck, D.; Sweet-Cordero, A.; Ebert, B. L.; Mak, R. H.; Ferrando, A. A.; Downing, J. R.; Jacks, T.; Horvitz, H. R.; Golub, T. R. MicroRNA Expression Profiles Classify Human Cancers. *Nature* **2005**, *435*, 834−838.

(9) Mitchell, P. S.; Parkin, R. K.; Kroh, E. M.; Fritz, B. R.; Wyman, S. K.; Pogosova-Agadjanyan, E. L.; Peterson, A.; Noteboom, J.; O'Briant, K. C.; Allen, A.; Lin, D. W.; Urban, N.; Drescher, C. W.; Knudsen, B. S.; Stirewalt, D. L.; Gentleman, R.; Vessella, R. L.; Nelson, P. S.; Martin, D. B.; Tewari, M. Circulating MicroRNAs as Stable Blood-based Markers for Cancer Detection. *Proc. Natl. Acad. Sci. U.S.A.* **2008**, *105*, 10513−10518.

(10) Croce, C. M. Causes and Consequences of MicroRNA Dysregulation in Cancer. *Nat. Rev. Genet.* **2009**, *10*, 704−714.

(11) Heegaard, N. H. H.; Schetter, A. J.; Welsh, J. A.; Yoneda, M.; Bowman, E. D.; Harris, C. C. Circulating Micro-RNA Expression Profiles in Early Stage Nonsmall Cell Lung Cancer. *Int. J. Cancer* **2012**, *130*, 1378−1386.

(12) Jiang, S.; Zhang, H.-W.; Lu, M.-H.; He, X.-H.; Li, Y.; Gu, H.; Liu, M.-F.; Wang, E.-D. MicroRNA-155 Functions as an OncomiR in Breast Cancer by Targeting the Suppressor of Cytokine Signaling 1 Gene. *Cancer Res.* **2010**, *70*, 3119−3127.

(13) Faraoni, I.; Antonetti, F. R.; Cardone, J.; Bonmassar, E. MiR-155 Gene: A Typical Multifunctional MicroRNA. *Biochim. Biophys. Acta, Mol. Basis Dis.* **2009**, *1792*, 497−505.

(14) Feng, Q.-M.; Shen, Y.-Z.; Li, M.-X.; Zhang, Z.-L.; Zhao, W.; Xu, J.-J.; Chen, H.-Y. Dual-Wavelength Electrochemiluminescence Ratiometry Based on Resonance Energy Transfer between Au Nanoparticles Functionalized g-C_3N_4 Nanosheet and $Ru(bpy)_3^{2+}$ for MicroRNA Detection. *Anal. Chem.* **2016**, *88*, 937−944.

(15) Azimzadeh, M.; Rahaie, M.; Nasirizadeh, N.; Ashtari, K.; Naderi-Manesh, H. An Electrochemical Nanobiosensor for Plasma MiRNA-155, Based on Graphene Oxide and Gold Nanorod, for Early Detection of Breast Cancer. *Biosens. Bioelectron.* **2016**, *77*, 99−106.

(16) Liu, L.; Shangguan, C.; Guo, J.; Ma, K.; Jiao, S.; Yao, Y.; Wang, J. Ultrasensitive SERS Detection of Cancer-Related miRNA-182 by MXene/MoS_2@AuNPs with Controllable Morphology and Optimized Self-Internal Standards. *Adv. Opt. Mater.* **2020**, *8*, 2001214.

(17) Zhang, Q.; Liu, S.; Du, C.; Fu, Y.; Xiao, K.; Zhang, X.; Chen, J. Highly Selective and Sensitive microRNA-210 Assay Based on Dual-

Signaling Electrochemical and Photocurrent-Polarity-Switching Strategies. *Anal. Chem.* **2021**, *93*, 14272−14279.
(18) Wang, M.; Yin, H.; Zhou, Y.; Sui, C.; Wang, Y.; Meng, X.; Waterhouse, G. I. N.; Ai, S. Photoelectrochemical Biosensor for MicroRNA Detection Based on a MoS_2/g-C_3N_4/black TiO_2 Heterojunction with Histostar@AuNPs for Signal Amplification. *Biosens. Bioelectron.* **2019**, *128*, 137−143.
(19) Li, H.; Han, M.; Weng, X.; Zhang, Y.; Li, J. DNA-Tetrahedral-Nanostructure-Based Entropy-Driven Amplifier for High-Performance Photoelectrochemical Biosensing. *ACS Nano* **2021**, *15*, 1710−1717.
(20) Low, S. S.; Chen, Z.; Li, Y.; Lu, Y.; Liu, Q. Design Principle in Biosensing: Critical Analysis Based on Graphitic Carbon Nitride (G-C_3N_4) Photoelectrochemical Biosensor. *TrAC, Trends Anal. Chem.* **2021**, *145*, 116454.
(21) Li, X.; Chen, C.; Yang, Y.; Lei, Z.; Xu, H. 2D Re-Based Transition Metal Chalcogenides: Progress, Challenges, and Opportunities. *Adv. Sci.* **2020**, *7*, 2002320.
(22) Dhenadhayalan, N.; Sriram, M. I.; Lin, K.-C. Aptamer-based Fluorogenic Sensing of Interferon-gamma Probed with ReS_2 and TiS_2 Nanosheets. *Sens. Actuators, B* **2018**, *258*, 929−936.
(23) Hu, H.; Zavabeti, A.; Quan, H.; Zhu, W.; Wei, H.; Chen, D.; Ou, J. Z. Recent Advances in Two-dimensional Transition Metal Dichalcogenides for Biological Sensing. *Biosens. Bioelectron.* **2019**, *142*, 111573.
(24) Yang, A.; Gao, J.; Li, B.; Tan, J.; Xiang, Y.; Gupta, T.; Li, L.; Suresh, S.; Idrobo, J. C.; Lu, T.-M.; Rong, M.; Koratkar, N. Humidity Sensing Using Vertically Oriented Arrays of ReS_2 Nanosheets Deposited on an Interdigitated Gold Electrode. *2D Mater.* **2016**, *3*, 045012.
(25) Martín-García, B.; Spirito, D.; Bellani, S.; Prato, M.; Romano, V.; Polovitsyn, A.; Brescia, R.; Oropesa-Nuñez, R.; Najafi, L.; Ansaldo, A.; D'Angelo, G.; Pellegrini, V.; Krahne, R.; Moreels, I.; Bonaccorso, F. Extending the Colloidal Transition Metal Dichalcogenide Library to ReS_2 Nanosheets for Application in Gas Sensing and Electrocatalysis. *Small* **2019**, *15*, No. e1904670.
(26) Liu, L.; Yao, Y.; Ma, K.; Shangguan, C.; Jiao, S.; Zhu, S.; Xu, X. Ultrasensitive Photoelectrochemical Detection of Cancer-related MiRNA-141 by Carrier Recombination Inhibition in Hierarchical Ti_3C_2@ReS_2. *Sens. Actuators, B* **2021**, *331*, 129470.
(27) Tang, Y.; Hao, H.; Kang, Y.; Liu, Q.; Sui, Y.; Wei, K.; Cheng, X. a.; Jiang, T. Distinctive Interfacial Charge Behavior and Versatile Photoresponse Performance in Isotropic/Anisotropic WS_2/ReS_2 Heterojunctions. *ACS Appl. Mater. Interfaces* **2020**, *12*, 53475−53483.
(28) Lv, J.; Liu, L. Direct Fabrication of Two-dimensional ReS_2 on SiO_2/Si Substrate by a Wide-temperature-range Atomic Layer Deposition. *Nanotechnology* **2019**, *31*, 055602.
(29) Hämäläinen, J.; Mattinen, M.; Mizohata, K.; Meinander, K.; Vehkamäki, M.; Räisänen, J.; Ritala, M.; Leskelä, M. Atomic Layer Deposition of Rhenium Disulfide. *Adv. Mater.* **2018**, *30*, 1703622.
(30) Liu, C.; Gillette, E. I.; Chen, X.; Pearse, A. J.; Kozen, A. C.; Schroeder, M. A.; Gregorczyk, K. E.; Lee, S. B.; Rubloff, G. W. An All-in-one Nanopore Battery Array. *Nat. Nanotechnol.* **2014**, *9*, 1031−1039.
(31) Mondal, S.; Kim, S. J.; Choi, C.-G. Honeycomb-like MoS_2 Nanotube Array-Based Wearable Sensors for Noninvasive Detection of Human Skin Moisture. *ACS Appl. Mater. Interfaces* **2020**, *12*, 17029−17038.
(32) Loh, K. P.; Zhang, H.; Chen, W. Z.; Ji, W. Templated Deposition of MoS_2 Nanotubules Using Single Source Precursor and Studies of Their Optical Limiting Properties. *J. Phys. Chem. B* **2006**, *110*, 1235−1239.
(33) Qin, J.-K.; Shao, W.-Z.; Xu, C.-Y.; Li, Y.; Ren, D.-D.; Song, X.-G.; Zhen, L. Chemical Vapor Deposition Growth of Degenerate p-Type Mo-Doped ReS_2 Films and Their Homojunction. *ACS Appl. Mater. Interfaces* **2017**, *9*, 15583−15591.
(34) Goodenough, J. B.; Kim, Y. Challenges for Rechargeable Li Batteries. *Chem. Mater.* **2009**, *22*, 587−603.
(35) Xu, X.; Zhao, H.; Wang, R.; Zhang, Z.; Dong, X.; Pan, J.; Hu, J.; Zeng, H. Identification of Few-layer ReS_2 as Photo-electro Integrated Catalyst for Hydrogen Evolution. *Nano Energy* **2018**, *48*, 337−344.
(36) Xu, J.; Fang, C.; Zhu, Z.; Wang, J.; Yu, B.; Zhang, J. Nanoscale Engineering and Mo-doping of 2D Ultrathin ReS_2 Nanosheets for Remarkable Electrocatalytic Hydrogen Generation. *Nanoscale* **2020**, *12*, 17045−17052.
(37) Abu-Sharkh, S.; Doerffel, D. Rapid Test and Non-linear Model Characterisation of Solid-state Lithium-ion Batteries. *J. Power Sources* **2004**, *130*, 266−274.
(38) Bae, C.; Kim, S.; Ahn, B.; Kim, J.; Sung, M. M.; Shin, H. Template-directed Gas-phase Fabrication of Oxide Nanotubes. *J. Mater. Chem.* **2008**, *18*, 1362−1367.
(39) Anson, F. C. Application of Potentiostatic Current Integration to the Study of the Adsorption of Cobalt(III)-Ethylenedinitrilo-(tetraacetate) on Mercury Electrodes. *Anal. Chem.* **1964**, *36*, 932−934.
(40) Enyashin, A. N.; Popov, I.; Seifert, G. Stability and Electronic Properties of Rhenium Sulfide Nanotubes. *Phys. Status Solidi B* **2009**, *246*, 114−118.
(41) Jin, Z.; Shin, S.; Kwon, D. H.; Han, S.-J.; Min, Y.-S. Novel Chemical Route for Atomic Layer Deposition of MoS_2 Thin Film on SiO_2/Si Substrate. *Nanoscale* **2014**, *6*, 14453.
(42) Mackus, A. J. M.; Schneider, J. R.; MacIsaac, C.; Baker, J. G.; Bent, S. F. Synthesis of Doped, Ternary, and Quaternary Materials by Atomic Layer Deposition: A Review. *Chem. Mater.* **2018**, *31*, 1142−1183.
(43) Liu, L.; Ma, K.; Xu, X.; Shangguan, C.; Lv, J.; Zhu, S.; Jiao, S.; Wang, J. MoS_2-ReS_2 Heterojunctions from a Bimetallic Co-chamber Feeding Atomic Layer Deposition for Ultrasensitive MiRNA-21 Detection. *ACS Appl. Mater. Interfaces* **2020**, *12*, 29074−29084.
(44) Yang, J.; Xu, X.; Liu, L. Plasma-assisted Friction Control of 2D MoS_2 Made by Atomic Layer Deposition. *Nanotechnology* **2020**, *31*, 395711.
(45) Sun, Q.; Zhang, B.; Diao, L.; Chen, B.; Song, K.; Ma, L.; He, F. Engineering the Electronic Structure of 1T′-ReS_2 Through Nitrogen Implantation for Enhanced Alkaline Hydrogen Evolution. *J. Mater. Chem. A* **2020**, *8*, 11607−11616.
(46) Zhang, T.; Jiang, B.; Xu, Z.; Mendes, R. G.; Xiao, Y.; Chen, L.; Fang, L.; Gemming, T.; Chen, S.; Rümmeli, M. H.; Fu, L. Twinned Growth Behaviour of Two-dimensional Materials. *Nat. Commun.* **2016**, *7*, 13911.
(47) Sneha, V. R.; Padma, N.; Yadav, R. A.; Jagannath; Girija, K. G.; Arvind, A.; Rao, R. Interlayer Coupling and Diode characteristics of Heterostructures of Solution Processed MoS_2:ReS_2 Nanocrystals. *Appl. Surf. Sci.* **2020**, *505*, 144475.
(48) Tan, S. J. R.; Sarkar, S.; Zhao, X.; Luo, X.; Luo, Y. Z.; Poh, S. M.; Abdelwahab, I.; Zhou, W.; Venkatesan, T.; Chen, W.; Quek, S. Y.; Loh, K. P. Temperature- and Phase-Dependent Phonon Renormalization in 1T'-MoS_2. *ACS Nano* **2018**, *12*, 5051−5058.
(49) Wadhwa, R.; Agrawal, A. V.; Kushavah, D.; Mushtaq, A.; Pal, S. K.; Kumar, M. Investigation of Charge Transport and Band Alignment of MoS_2-ReS_2 Heterointerface for High Performance and Self-driven Broadband Photodetection. *Appl. Surf. Sci.* **2021**, *569*, 150949.
(50) Wang, W.; Zeng, X.; Warner, J. H.; Guo, Z.; Hu, Y.; Zeng, Y.; Lu, J.; Jin, W.; Wang, S.; Lu, J.; Zeng, Y.; Xiao, Y. Photoresponse-Bias Modulation of a High-Performance MoS_2 Photodetector with a Unique Vertically Stacked 2H-MoS_2/1T@2H-MoS_2 Structure. *ACS Appl. Mater. Interfaces* **2020**, *12*, 33325−33335.
(51) Sreeparvathy, P. C.; Kanchana, V.; Anees, P.; Vaitheeswaran, G. Emergence of Strain Induced Two Dimensional Metallic State in ReS_2. *J. Solid State Chem.* **2019**, *269*, 138−144.
(52) Shi, W.; Wang, Z.; Fu, Y. Q. Rhenium Doping Induced Structural Transformation in Mono-layered MoS_2 with Improved Catalytic Activity for Hydrogen Evolution Reaction. *J. Phys. D: Appl. Phys.* **2017**, *50*, 405303.
(53) Oh, I.-K.; Kim, W.-H.; Zeng, L.; Singh, J.; Bae, D.; Mackus, A. J. M.; Song, J.-G.; Seo, S.; Shong, B.; Kim, H.; Bent, S. F. Synthesis of a

Hybrid Nanostructure of ZnO-Decorated MoS_2 by Atomic Layer Deposition. *ACS Nano* **2020**, *14*, 1757−1769.
(54) Shim, J.; Oh, S.; Kang, D.-H.; Jo, S.-H.; Ali, M. H.; Choi, W.-Y.; Heo, K.; Jeon, J.; Lee, S.; Kim, M.; Song, Y. J.; Park, J.-H. Phosphorene/rhenium Disulfide Heterojunction-based Negative Differential Resistance Device for Multi-valued Logic. *Nat. Commun.* **2016**, *7*, 13413.
(55) Guo, Y.; Robertson, J. Band Engineering in Transition Metal Dichalcogenides: Stacked Versus Lateral Heterostructures. *Appl. Phys. Lett.* **2016**, *108*, 233104.
(56) Britnell, L.; Ribeiro, A.; Jalil, R.; Belle, B. D.; Mishchenko, A.; Kim, Y.-J.; Gorbachev, R. V.; Georgiou, T.; Morozov, S. V.; Grigorenko, A. N.; Geim, A. K.; Casiraghi, C.; Neto, A. H. C.; Novoselov, K. S. Strong Light-Matter Interactions in Heterostructures of Atomically Thin Films. *Science* **2013**, *340*, 1311−1314.
(57) Zhang, J.; Shang, M.; Gao, Y.; Yan, J.; Song, W. High-performance VS_2 QDs-based Type II Heterostructured Photoanode for Ultrasensitive Aptasensing of Lysozyme. *Sens. Actuators, B* **2020**, *304*, 127411.
(58) Shim, J.; Kang, D.-H.; Kim, Y.; Kum, H.; Kong, W.; Bae, S.-H.; Almansouri, I.; Lee, K.; Park, J.-H.; Kim, J. Recent Progress in Van der Waals (vdW) Heterojunction-based Electronic and Optoelectronic Devices. *Carbon* **2018**, *133*, 78−89.
(59) Liu, D.; Yang, G.; Zhang, X.; Chen, S.; Yuan, R. A Novel Potential-regulated Ratiometric Electrochemiluminescence Sensing Strategy Based on Poly(9,9-di-n-octylfluorenyl-2,7-diyl) Polymer Nanoparticles for MicroRNA Detection. *Sens. Actuators, B* **2021**, *329*, 129210.
(60) Wang, L.; Zhao, K.-R.; Liu, Z.-J.; Zhang, Y.-B.; Liu, P.-F.; Ye, S.-Y.; Zhang, Y.-W.; Liang, G.-X. An "On-off" Signal-switchable Electrochemiluminescence Biosensor for Ultrasensitive Detection of Dual MicroRNAs Based on DNAzyme-powered DNA Walker. *Sens. Actuators, B* **2021**, *348*, 130660.
(61) Zhuang, T.; Zhang, H.; Wang, L.; Yu, L.; Wang, Z. Anchoring Luminol Based on Ti_3C_2-mediated in Situ Formation of Au NPs for Construction of an Efficient Probe for MiRNA Electrogenerated Chemiluminescence Detection. *Anal. Bioanal. Chem.* **2021**, *413*, 6963−6971.
(62) Cao, Z.; Duan, F.; Huang, X.; Liu, Y.; Zhou, N.; Xia, L.; Zhang, Z.; Du, M. A Multiple Aptasensor for Ultrasensitive Detection of MiRNAs by Using Covalent-organic Framework Nanowire as Platform and Shell-encoded Gold Nanoparticles as Signal Labels. *Anal. Chim. Acta* **2019**, *1082*, 176−185.
(63) Liu, L.; Zhu, S.; Wei, Y.; Liu, X.; Jiao, S.; Yang, J. Ultrasensitive Detection of MiRNA-155 Based on Controlled Fabrication of AuNPs@MoS_2 Nanostructures by Atomic Layer Deposition. *Biosens. Bioelectron.* **2019**, *144*, 111660.
(64) Yang, X.; Feng, M.; Xia, J.; Zhang, F.; Wang, Z. An electrochemical Biosensor Based on AuNPs/Ti_3C_2 MXene Three-dimensional Nanocomposite for MicroRNA-155 Detection by Exonuclease III-aided Cascade Target Recycling. *J. Electroanal. Chem.* **2020**, *878*, 114669.
(65) Meng, L.; Li, Y.; Yang, R.; Zhang, X.; Du, C.; Chen, J. A Sensitive Photoelectrochemical Assay of MiRNA-155 Based on a CdSe QDs//NPC-ZnO Polyhedra Photocurrent-direction Switching System and Target-triggered Strand Displacement Amplification Strategy. *Chem. Commun.* **2019**, *55*, 2182−2185.
(66) Jiao, S.; Liu, L.; Wang, J.; Ma, K.; Lv, J. A Novel Biosensor Based on Molybdenum Disulfide (MoS_2) Modified Porous Anodic Aluminum Oxide Nanochannels for Ultrasensitive microRNA-155 Detection. *Small* **2020**, *16*, 2001223.
(67) Liu, H.; Ai, S.; Liu, Y.; Zeng, H.; Da, H.; Liu, Y.; Chai, Y.; Yuan, R. Enhancing Photoelectrochemical Performance of $ZnIn_2S_4$ by Phosphorus Doping for Sensitive Detection of MiRNA-155. *Chem. Commun.* **2020**, *56*, 14275−14278.

https://doi.org/10.1021/acsami.1c23009
ACS Appl. Mater. Interfaces 2022, 14, 10081−10091